Nano Research
DOI 10.1007/s12274-016-1044-7
Research Article
ISSN 1998-0124
CN 11-5974/O4

Dual response of graphene-based ultra-small molecular junctions to defect engineering

Kunpeng Dou[1], Xiaoxiao Fu[1], Abir De Sarkar[2], and Ruiqin Zhang[1] (✉)

[1] *Department of Physics and Materials Science, City University of Hong Kong, Hong Kong, China*
[2] *Institute of Nano Science and Technology (An Autonomous Institute of Department of Science and Technology, Government of India), Habitat Centre (Transit Campus), Phase X, Sector-64, Mohali, Punjab-160 062, India*

Received: 21 November 2015
Revised: 17 January 2016
Accepted: 8 February 2016

KEYWORDS
graphene,
defect,
electron transport,
molecular electronics,
single-molecule studies

ABSTRACT

It has been reported that N and B doping induce a quasi-bound state that suppresses the conduction in graphene nanoribbon (GNR)-based junctions, while an H defect or a pyridine-like N-atom (PN) substitution at the edge of the GNR does not affect the transmission close to the Fermi energy. However, these results may vary when the size of the functional unit of the GNR junction decreases to a molecular level. In this study, a defect is introduced to a test-bed architecture consisting of a polyacene bridging two zigzag GNR electrodes, which changes the molecular state alignment and coupling to the electrode states, and varies the equivalence between two eigen-channels at the Fermi level. It is revealed that B and N atom substitution, and H defects play a dual role in the molecular conductance, whereas the PN substitution acts as an ineffective dopant. The results obtained from density functional theory combined with the non-equilibrium Green's function method aid in determining the optimal design for the GNR-based ultra-small molecular devices via defect engineering.

1 Introduction

Defect engineering, such as impurity doping [1, 2] or H defects [3–5], is of paramount importance in quantum information processing in conventional Si electronics. Therefore, it is not surprising that this operating principle has also inspired substantial efforts to introduce defects in carbon materials, thereby encoding and transferring information through an even denser, faster, and more efficient circuitry than a Si-based one. For example, N (or B) impurity doping in carbon nanotubes (CNTs) [6–8] can induce a quasi-bound donor (or acceptor) state, which leads to a total quantum blockade above (or below) the Fermi level [6]. In comparison, N and B doping exhibit stronger features in graphene nanoribbons (GNRs), depending on the position of the dopant, ribbon width, symmetry, etc. [9–14]. In particular, Martins et al. showed that B doping can weakly (strongly) reduce the spin-down (up) transmission channels in zigzag GNRs (ZGNRs),

Address correspondence to aprqz@cityu.edu.hk

and that such anisotropy could be magnified by decreasing the width of the nanoribbons or by increasing the amount of doping atoms [9]. Blanca et al. observed that when the impurity preserves the mirror symmetry in armchair GNRs, no backscattering is obtained during the transport process [10]. They also demonstrated that doped ZGNRs exhibit an unusual acceptor–donor transition. Yu et al. showed that the impurity state caused by N in ZGNRs could appear either above or below the Fermi level depending on the position of the dopant [11]. Similar findings were obtained by Blanca et al. when they examined the effect of B doping in ZGNRs [10]. Li et al. reported that a single N-atom substitution transforms an antiferromagnetic semiconducting ZGNR into a spin gapless semiconductor, while a double edge substitution produces a metallic N-doped graphene [12]. They also showed that a pyridine-like N (PN) [7, 12] has little influence on the edge states of ZGNRs. Furthermore, Martins et al. confirmed that an H defect at the edges of the GNRs can introduce localized σ states far from the Fermi level and does not affect the transmission coefficient of the tunnel junction close to the Fermi energy [14]. Along this line, challenges in the preparation of efficient and reliable GNR-based devices via defect engineering can still be expected. For example, to meet the demand for further miniaturization, the size of the functional block of the GNR junction is required to decrease to a molecular level, where our understanding of the defect engineering is still in its infancy. To explore this issue, we have shrunk the device component of a ZGNR-based junction to its ultimate size limit, polyacene (PA) molecules, and have introduced a defect as a test-bed structure.

In this study, the influence of impurity doping (including single B- and N-atom substitution, and PN substitution) and H defects on the conductance characteristics of a PA containing two to eight aromatic carbon rings, denoted hereafter by PA2 to PA8, were investigated. ZGNRs with six zigzag chains were used as electrodes. The PA represents a fragment of the π-bonded carbon network of the electrode, and consequently it is incorporated into the junction by seamless coupling. The junction with a PA8 in the device region is selected as an example in Fig. 1 to schematically show the two-probe transport system: U1–U4 (A sub-lattice) and D1–D4 (B sub-lattice) denote the doping positions for a single B and N-atom substitution. U1–U4 positions also correspond to the H defect and PN substitution. The marked positions U and D in Fig. 1 show all the non-equivalent positions for doping the PA with a single-atom or an H defect.

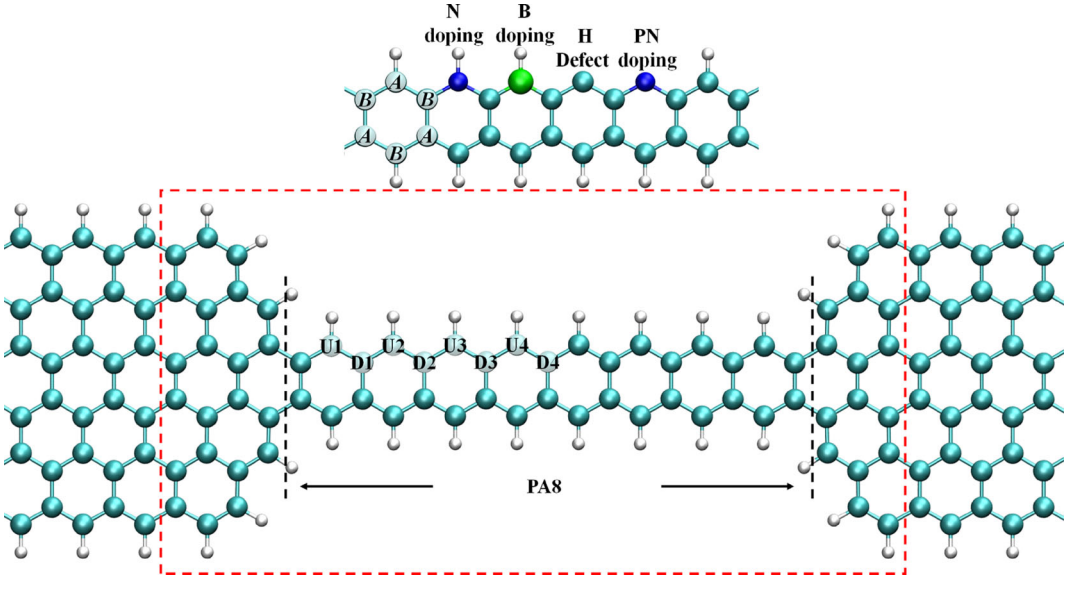

Figure 1 Schematic illustration of the two-probe system with a PA8 containing eight-fused benzene rings in the central region. There are two types of sub-lattice carbon atoms in the junction: A and B. U1–U4 (A sub-lattice) and D1–D4 (B sub-lattice) represent the doping positions for a single B and N atom substitution; U1–U4 also represent the positions for an H defect and PN substitution. The part in the red box corresponds to the device region.

2 Results and discussion

Before studying the effect of defect engineering on the molecular conductance, it is necessary to first clarify the conductance features of pristine PA. The equilibrium conductance is given by Eq. (1).

$$G = T(E_f) \times G_0 \quad (1)$$

where $T(E)$ is the transmission spectrum, E_f is the Fermi energy, and $G_0 = 2e^2/h$ is the conductance quantum [15]. The black solid circles in Fig. 2 represent the conductance of pristine junctions. It is interesting to note that the molecular conductance does not decrease exponentially with the molecular length, which is normally associated with tunneling [16], but it increases gradually from PA2 to PA8 [17].

To explore this unusual length-dependent conductance, we studied the zero-bias transmission spectra (black curves) of pristine PA3, PA5, and PA8 shown in Figs. 3(a1), 3(b1), and 3(c1). For each system, three transmission resonances contribute to the conductance. One is situated at the E_f while the other two are more distant, as indicated by the black arrows. As the molecular length increases from PA3 to PA8, the latter two resonances gradually approach the E_f. The large overlap in the tails of these two resonances enhances the transmission coefficient at the E_f for longer PA molecules. This facilitates the increase in junction conductance with the increase in length.

To determine the origin of the three transmission peaks, the projected density of states (PDOS) on the molecule and electrode is plotted in Figs. 3(a2), 3(b2), and 3(c2). For the three junctions, one significant peak distributes around the E_f on the PDOS of the electrode. The transmission peak at the E_f is attributable to the electrode edge states, and it results in hybridization

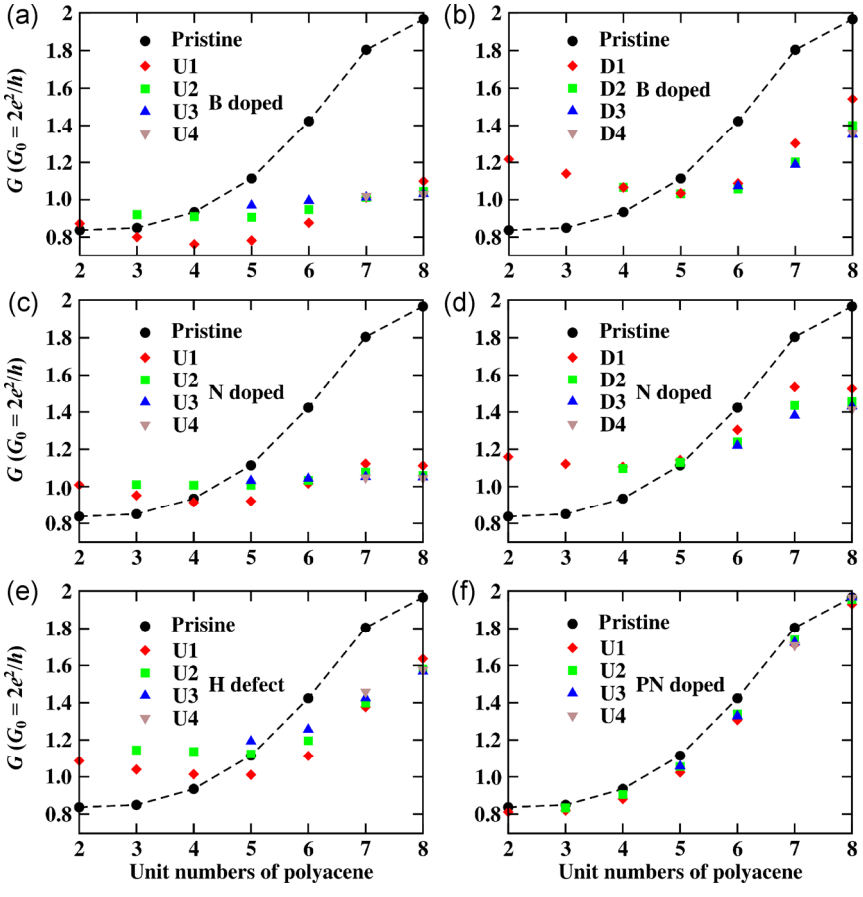

Figure 2 Equilibrium conductance of the PA-based series with aromatic rings from two to eight: (a) and (b) single B-atom substitution at U positions (A sub-lattice) and D positions (B sub-lattice); (c) and (d) single N-atom substitution at U positions (A sub-lattice) and D positions (B sub-lattice); (e) H defect; (f) PN-doped.

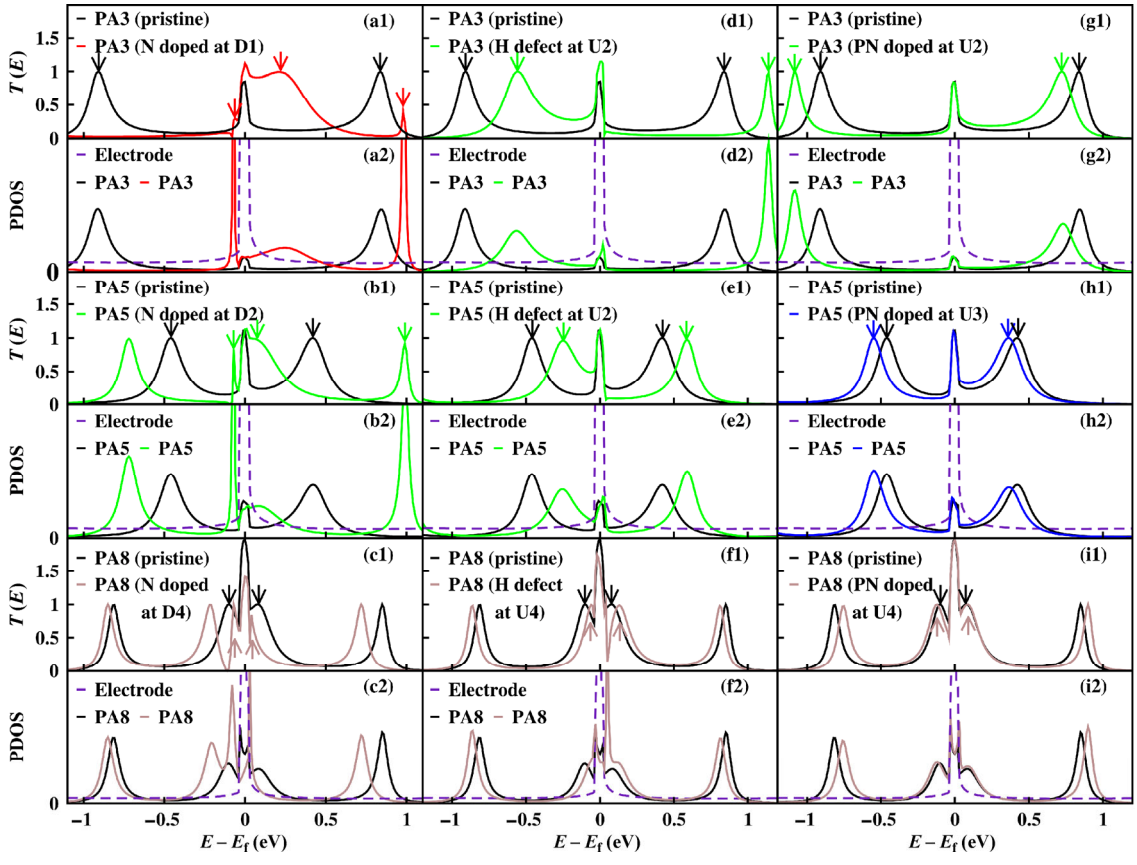

Figure 3 Transmission spectra and PDOS of the PA-based series. PA with a single N-atom substitution: (a1) and (a2) PA3 (doped at D1); (b1) and (b2) PA5 (doped at D2); (c1) and (c2) PA8 (doped at D4). PA with an H defect: (d1) and (d2) PA3 (defect at U2); (e1) and (e2) PA5 (defect at U2); (f1) and (f2) PA8 (defect at U4). PA with PN doping: (g1) and (g2) PA3 (doped at U2); (h1) and (h2) PA5 (doped at U5); (i1) and (i2) PA8 (doped at U4). The colors of the transmission spectra and PDOS for the PA correlate with those in Fig. 2.

with states of the PA molecule. On the other hand, the two peaks on the PDOS of the molecules near the E_f, correspond to the renormalized highest occupied molecular orbital (HOMO) and lowest unoccupied molecular orbital (LUMO) [18], and distribute at the same energies of the two mentioned transmission peaks, distant from the E_f. The good correlation between the PDOS and the transmission function indicates that the conductance of pristine PA can be regarded as a superposition of resonances derived from one electrode and two molecular states, namely, the HOMO and LUMO. Since all the junctions possess the same electrode geometry, the unusual length-dependent conductance for pristine PA is probably correlated with the intrinsic electronic properties of the molecule, particularly, the molecular state alignment, and its coupling strength to the electrode states. To demonstrate the evolution of the HOMO and LUMO in various pristine PA molecules, the peaks corresponding to these resonances (indicated by black arrows in Figs. 3(a1), 3(b1), and 3(c1)) have been extracted and plotted in Fig. 4 (solid black squares). Pristine PA shows a progressive shift of the molecular states with respect to the E_f as the length increases. In addition, the broadening of the HOMO and LUMO derived resonances varies slightly with the PA length. These two factors lead to a higher conductance for longer PA molecules.

The impact of defect engineering was then studied. The doping position or H defects have been systematically varied to study the resulting variation in conductance with respect to the pristine material discussed above. In particular, their impact can be classified into three groups as follows.

Firstly, in Figs. 2(a)–2(d), the conductance of PA upon B and N doping shows a clear deviation from

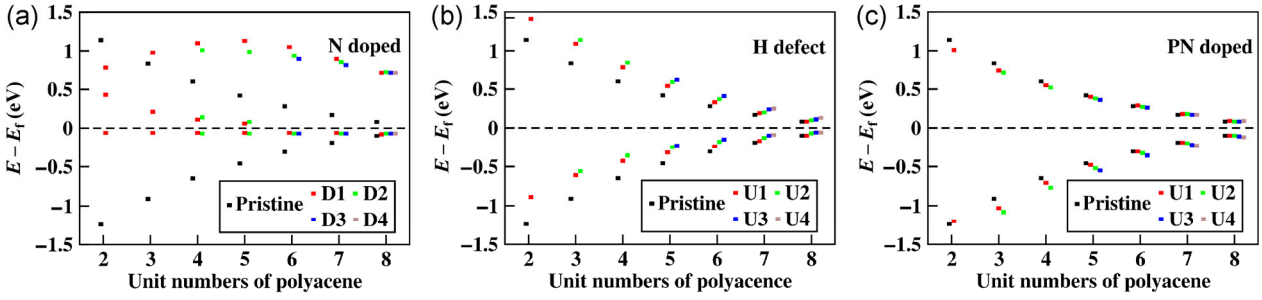

Figure 4 Energy positions of the transmission peaks derived from molecular states: (a) single N-atom substitution at D positions; (b) H defect; (c) PN-doped. The black solid squares correspond to pristine systems.

the pristine material. In particular, single B- and N-atom substitution play two clear and opposite roles in molecular conductance: When the length of the PA is longer than a certain value, the dopant always suppresses the conductance, but when the length is shorter than this value, the impurity enhances the conductance. Thus, doping results in a turning point in conductance at this critical length. The transition in conductance induced by B doping at the D position is revealed at PA5 with no apparent transition caused by doping at the U position. The transition imparted by N doping at the U and D positions occurs at PA4 and PA5, respectively. As previously reported, B and N impurity doping suppress the transmission on CNTs [6–8] and GNRs [9–14], and no transition in conductance is observed on these systems. Hence, it is clear that B and N doping influence in a different and complex manner the conductance of a GNR-based molecular junction shrunk to an ultra-small scale.

Secondly, analogous to the single B and N doping, the H defect also induces a transition in conductance at PA5 in Fig. 2(e). In addition, at this length, an H defect-induced transition in conductance also occurs when it moves from the U1 to U3 position. The situation in this case is clearly different from that in GNRs, where an H defect has no perturbative effect on the transmission coefficient around the E_f [14].

Thirdly, the resultant PN doping-induced conductance [7] is quite similar in magnitude to its pristine counterpart, as shown in Fig. 2(f). Again, the PN substitution is ineffective as dopant, and the response of the PA-based junction resembles that of ZGNRs [7].

We then studied the origin of the conductance response for the three groups. The combined transmission spectra and PDOS analysis (colored curves) are shown in Fig. 3. For each defective system, the transmission resonances (except the one at the E_f) contributing to the conductance are denoted by colored arrows. The corresponding PDOS analysis shows that these transmission peaks originate from one electrode state (located at the E_f) and several molecular state-derived resonances. Since the junctions possess an identical electrode structure, we focused on the molecular state-derived resonances for the three defective groups.

To illustrate the first group, we used N doping at the D position as a representative example. For the PA3 with N doped at D1, as shown in Fig. 3(a1), there is one resonance derived from a molecular state, immediately above the E_f. The tail of this resonance contributes greatly to the conductance. It moves closer to the E_f for the PA5 with N doped at D2 in Fig. 3(b1), but the broadening decreases indicating a reduced coupling of the electrode states. For the PA8 with N doped at D4, seen in Fig. 3(c1), this resonance is even closer to the E_f, and almost merges with the electrode state-derived resonance, decreasing its broadening even further. For the B-doped series, the corresponding resonance making a dominant contribution to the conductance is located immediately below the E_f (Fig. S3 in the Electronic Supplementary Material (ESM)). It also moves closer to the E_f and its broadening decreases with the increase in molecular length. To clarify the molecular state alignment with respect to the E_f in greater detail, the energy positions of the transmission peaks (indicated by colored arrows in Fig. 3) are extracted and plotted in Fig. 4. For the N-doped systems, the molecular state-derived resonances distribute mainly near and above the E_f in Fig. 4(a), while for the B-doped ones, these resonances distribute

mainly near and below the E_f (Fig. S4 in the ESM). The transition in conductance caused by single B and N doping could be the result of a length-dependent variation in the molecular level alignment and its coupling strength to the electrode states.

Concerning the second group, for the PA3 with an H defect at U2, as shown in Fig. 3(d1), the tail of the HOMO resonance makes a significant contribution to the conductance. This resonance moves gradually closer to the E_f with increasing molecular length, as shown in Figs. 3(e1) and 3(f1). Its broadening clearly decreases for the PA8 with a defect at U4. The details of the molecular level alignment is shown in Fig. 4(b). These states shift to higher energies compared to their pristine counterparts. Similar to single B and N doping, length-dependent variations in the molecular state alignment and its coupling strength to the electrode states produce an H defect-induced transition in conductance with the variation in the molecular length. The coupling strength is estimated from the broadening of the molecular state derived transmission resonances. Furthermore, for the PA5 with an H defect at different U positions, the coupling strength between the molecular and electrode states remains relatively unchanged and the molecular state alignment has a greater influence on the transport behavior. When the H defect moves from the U1 to the U3 position, the HOMO of the PA5 contributing significantly to the conductance, shifts gradually closer to the E_f and this determines the H defect-induced transition in conductance with the variation in the defect position.

For the third group, since the molecular length of the PN-doped system increases from PA3 to PA8, no noticeable variations in the broadening of the molecular resonances were observed. Furthermore, the energy levels of the HOMO and LUMO shown in Fig. 4(c) deviate slightly from their pristine counterparts. The weak length-dependent variation in the molecular state alignment and its coupling strength to the electrode states are responsible for the undoped characteristics of the PN substitution in the PA-based junction.

Thus far, the origin of the conductance response to defect engineering has been discussed qualitatively by length-dependent (position-dependent defects) variations in the molecular state alignment and its coupling to the electrode states. To achieve both a quantitative and deeper understanding, it is necessary to investigate the evolution of the transmission eigen-channels with respect to the molecular length [19]. At zero-bias, the equilibrium conductance of each junction is characterized by two eigen-channels as listed in Table 1. It should be noted that the transmission coefficients, T_1 and T_2, of the two channels are nearly equal for pristine cases. This kind of equivalence is typical of pristine junctions. The two channels are affected differently by defect engineering as follows.

For the first group, upon N doping, T_1 and T_2 are revealed to contribute differently to the conductance. It is crucial to note that the different responses of the two eigen-channels to N doping determine the transition in conductance of the system. For the PA3, compared to the pristine systems, the increase in T_1, 0.527 (0.513), is larger than the decrease in T_2, 0.255 (0.353), for N doping at the D1 (U2) position. This results in

Table 1 Decomposed transmission eigen-channels for the PA-based series with various defects

	Pristine			B doped			N doped					
Polyacene	PA3	PA5	PA8	PA3	PA5	PA8	PA3	PA4	PA8	PA3	PA5	PA8
Doping position		none		D1	D2	D4	U2	U1	U4	D1	D2	D4
Channel 1(T_1)	0.444	0.578	0.997	0.957	0.833	0.933	0.957	0.852	1	0.971	0.906	0.997
Channel 2(T_2)	0.406	0.537	0.968	0.183	0.198	0.423	0.054	0.061	0.046	0.151	0.224	0.418

	H defect					PN doped		
Polyacene	PA3	PA5			PA8	PA3	PA5	PA8
Defect or Doping position	U2	U1	U2	U3	U4	U2	U3	U4
Channel 1(T_1)	0.979	0.780	0.906	0.981	0.987	0.573	0.663	0.996
Channel 2(T_2)	0.165	0.231	0.217	0.211	0.589	0.262	0.394	0.969

an overall enhancement of the conductance upon N doping. As the number of aromatic rings increases to five (four), the opposite effects from the two eigen-channels cancel each other for N doping at D2 (U1). Therefore, the doped conductance appears to replicate the pristine one. The length of the PA5 (PA4) is regarded as the critical value for the transition in conductance via N doping at the D (U) position. Finally, as the number of aromatic rings increases to eight, there is almost no variation in T_1, while T_2 is nearly halved for N doping at D4 (U4) with respect to the pristine counterpart. Consequently, N doping suppresses the conductance. The origin of the conductance variations on B-doped systems is similar to that on N-doped ones: The two eigen-channels contribute differently, as listed in Table 1.

For the second group, as listed in Table 1, the H defect-induced transition in conductance due to the variation in the molecular length also originates from different variations in the length dependence of the two channels, as for the B and N doping discussed above. Additionally, the same analysis could be performed in the case where the position of the H defect moves from U1 to U3.

For the third group, upon PN substitution for PA3, the difference in contribution between the two channels is not very large, unlike the two groups above. In comparison to the pristine counterpart, the increase of T_1 for the PA3 and PA5 is balanced by the decrease of T_2, and consequently, the conductance imparted by doping reaches that of its pristine counterpart. For the PA8, upon PN substitution, T_1 and T_2 both approach the ballistic value, as shown in the pristine system. Consequently, the PN-doped conductance nearly replicates that of the pristine one.

The details of the variation on isosurface of the transmission eigen-channels for three groups are shown in Fig. S5 (see the ESM).

The benchmark studies of electron transport in carbon materials (CNT [6], ZGNR [10], and other references in the introduction) have shown that impurity doping only suppresses the conductance. No other role of impurity doping has been considered or explored. In contrast, we studied the dual role of defects in GNR-based ultra-small molecular junctions following the model and methods previously reported [10]. In addition, we have also verified four factors carefully: broader electrodes, less symmetric setup, wider junctions compared to PA, and dopants distributed outside the junction. The detailed results are shown in the ESM. Our results confirm that these four factors do not alter the conclusion that defects play a dual role in the molecular conductance.

Given the recent achievements in experimental studies [20–25], both bottom-up [20] and top-down [25] techniques are capable of fabricating GNR-based junctions with an atomic precision. GNR heterojunctions consisting of seven and thirteen rows of carbon atoms have already been prepared experimentally [26]. Single-atom doping is controllable, thus ensuring the feasibility of defect engineering [27–29]. Ballistic transport in epitaxial GNR has been enabled [30] and various carbon-based devices have been developed [31–34], which circumvent the use of foreign metallic contacts with undesirable interfacial issues. All these studies confirm the experimental feasibility of designing the structures proposed in this study.

3 Conclusions

The texture of a defect is complex, and it can have counterintuitive consequences for the carrier transport at a molecular level. The molecular transport behavior is determined by variations in the molecular state alignment and its coupling to the electrode states. We hypothesize that the dual roles of defect engineering may be detected for GNR-based integrated circuits once an active device unit reaches the molecular level, where quantum interference effects are dominant [35]. In view of the metal–molecule–metal junction with multiple molecular wires, the inter-wire distance is a crucial parameter to generate an instructive or destructive interference that affects the conductance [36]. In comparison, defect engineering in GNR-based carbon devices presents new challenges to understand its dual role. Nevertheless, it offers the opportunity to design high-precision electronic devices in the future.

4 Methods

All the scattering regions were relaxed using density functional theory (DFT) as implemented in the SIESTA

package [37], before studying their transport properties. Optimization calculations were performed within the Ceperley-Alder local density approximation [38] and an energy cut-off of 150 Ry was used. Valence electrons were expanded in Double-ζ plus polarization and structural relaxations were allowed until the force acting on each atom reached less than 0.01 eV/Å. Then, the transport calculations were performed using DFT combined with the non-equilibrium Green's function [15] formalism as implemented in the TRANSIESTA package [39]. We performed test calculations to replicate the study previously reported [10], which showed a good agreement (Fig. S1 in the ESM). In addition, the analysis of the formation energy is given in Fig. S2 (see the ESM).

Acknowledgements

The work described in this paper was supported by a grant from the Research Grants Council of Hong Kong SAR (No. HKBU 12301814). The authors thank Wei Fan for discussion at the early stages of this work.

Electronic Supplementary Material: Supplementary material (further details of test calculation, relative formation energy, analysis for B-doped series, Transmission eigenchannel analysis and extension with more complex factors) is available in the online version of this article at http://dx.doi.org/10.1007/s12274-016-1044-7.

References

[1] Fukata, N. Impurity doping in silicon nanowires. *Adv. Mater.* **2009**, *21*, 2829–2832.

[2] Pierre, M.; Wacquez, R.; Jeh, X.; Sanquer, M.; Vinet, M.; Cueto, O. Single-donor ionization energies in a nanoscale CMOS channel. *Nat. Nanotechnol.* **2010**, *5*, 133–137.

[3] Kepenekian, M.; Robles, R.; Joachim, C.; Lorente, N. Surface-state engineering for interconnects on H-passivated Si(100). *Nano Lett.* **2013**, *13*, 1192–1195.

[4] Jelínek, P.; Švec, M.; Pou, P.; Perez, R.; Cháb, V. Tip-induced reduction of the resonant tunneling current on semiconductor surfaces. *Phys. Rev. Lett.* **2008**, *101*, 176101.

[5] Dou, K. P.; Fan, W.; Niehaus, T. A.; Frauenheim, T.; Wang, C. L.; Zhang, X. H.; Zhang, R. Q. Electron transport suppression from tip-π state interaction on Si(100)-2×1 surfaces. *J. Chem. Theory Comput.* **2011**, *7*, 707–712.

[6] Choi, H. J.; Ihm, J.; Louie, S. G.; Cohen, M. L. Defects, quasibound states, and quantum conductance in metallic carbon nanotubes. *Phys. Rev. Lett.* **2000**, *84*, 2917–2920.

[7] Yang, S. H.; Shin, W. H.; Kang, J. K. The nature of graphite- and pyridinelike nitrogen configurations in carbon nitride nanotubes: Dependence on diameter and helicity. *Small* **2008**, *4*, 437–441.

[8] Yu, S. S.; Zheng, W. T. Effect of N/B doping on the electronic and field emission properties for carbon nanotubes, carbon nanocones, and graphene nanoribbons. *Nanoscale* **2010**, *2*, 1069–1082.

[9] Martins, T. B.; Miwa, R. H.; da Silva, A. J. R.; Fazzio, A. Electronic and transport properties of boron-doped graphene nanoribbons. *Phys. Rev. Lett.* **2007**, *98*, 196803.

[10] Biel, B.; Blase, X.; Triozon, F.; Roche, S. Anomalous doping effects on charge transport in graphene nanoribbons. *Phys. Rev. Lett.* **2009**, *102*, 096803.

[11] Yu, S. S.; Zheng, W. T.; Wen, Q. B.; Jiang, Q. First principle calculations of the electronic properties of nitrogen-doped carbon nanoribbons with zigzag edges. *Carbon* **2008**, *46*, 537–543.

[12] Li, Y. F.; Zhou, Z.; Shen, P. W.; Chen, Z. F. Spin gapless semiconductor-metal-half-metal properties in nitrogen-doped zigzag graphene nanoribbons. *ACS Nano* **2009**, *3*, 1952–1958.

[13] Wang, H. B.; Maiyalagan, T.; Wang, X. Review on recent progress in nitrogen-doped graphene: Synthesis, characterization, and its potential applications. *ACS Catal.* **2012**, *2*, 781–794.

[14] Martins, T. B.; da Silva, A. J. R.; Miwa, R. H.; Fazzio, A. σ- and π-defects at graphene nanoribbon edges: Building spin filters. *Nano Lett.* **2008**, *8*, 2293–2298.

[15] Datta, S. *Electronic Transport in Mesoscopic Systems*; Cambridge University Press: New York, 1995.

[16] Nitzan, A. Electron transmission through molecules and molecular interfaces. *Ann. Rev. Phys. Chem.* **2001**, *52*, 681–750.

[17] Visontai, D.; Grace, I. M.; Lambert, C. J. Electron transport through ribbonlike molecular wires calculated using density-functional theory and Green's function formalism. *Phys. Rev. B* **2010**, *81*, 035409.

[18] Larade, B. J.; Taylor, J.; Zheng, Q. R.; Mehrez, H.; Pomorski, P.; Guo, H. Renormalized molecular levels in a $Sc_3N@C_{80}$ molecular electronic device. *Phys. Rev. B* **2001**, *64*, 195402.

[19] Paulsson, M.; Brandbyge, M. Transmission eigenchannels from nonequilibrium Green's functions. *Phys. Rev. B* **2007**, *76*, 115117.

[20] Cai, J. M.; Ruffieux, P.; Jaafar, R.; Bieri, M.; Braun, T.; Blankenburg, S.; Muoth, M.; Seitsonen, A. P.; Saleh, M.; Feng, X. L. et al. Atomically precise bottom-up fabrication of graphene nanoribbons. *Nature* **2010**, *466*, 470–473.

[21] Datta, S. S.; Strachan, D. R.; Khamis, S. M.; Johnson, A. T. C. Crystallographic etching of few-layer graphene. *Nano Lett.* **2008**, *8*, 1912–1915.

[22] Zhang, L. M.; Diao, S.; Nie, Y. F.; Yan, K.; Liu, N.; Dai, B. Y.; Xie, Q.; Reina, A.; Kong, J.; Liu, Z. F. Photocatalytic patterning and modification of graphene. *J. Am. Chem. Soc.* **2011**, *133*, 2706–2713.

[23] Martínez-Galera, A. J.; Brihuega, I.; Gutiérrez-Rubio, A.; Stauber, T.; Gómez-Rodríguez, J. M. Towards scalable nano-engineering of graphene. *Sci. Rep.* **2014**, *4*, 7314.

[24] Tapasztó, L.; Dobrik, G.; Lambin, P.; Biró, L. P. Tailoring the atomic structure of graphene nanoribbons by scanning tunnelling microscope lithography. *Nat. Nanotechnol.* **2008**, *3*, 397–401.

[25] Merino, P.; Švec, M.; Martinez, J. I.; Jelinek, P.; Lacovig, P.; Dalmiglio, M.; Lizzit, S.; Soukiassian, P.; Cernicharo, J.; Martin-Gago, J. A. Graphene etching on SiC grains as a path to interstellar polycyclic aromatic hydrocarbons formation. *Nat. Commun.* **2014**, *5*, 3054.

[26] Chen, Y.-C.; Cao, T.; Chen, C.; Pedramrazi, Z.; Haberer, D.; de Oteyza, D. G.; Fischer, F. R.; Louie, S. G.; Crommie, M. F. Molecular bandgap engineering of bottom-up synthesized graphene nanoribbon heterojunctions. *Nat. Nanotechnol.* **2015**, *10*, 156–160.

[27] Wang, H. T.; Wang, Q. X.; Cheng, Y. C.; Li, K.; Yao, Y. B.; Zhang, Q.; Dong, C. Z.; Wang, P.; Schwingenschlög, U.; Yang, W. et al. Doping monolayer graphene with single atom substitutions. *Nano Lett.* **2012**, *12*, 141–144.

[28] Guo, B. D.; Liu, Q.; Chen, E. D.; Zhu, H. W.; Fang, L.; Gong, J. R. Controllable N-doping of graphene. *Nano Lett.* **2010**, *10*, 4975–4980.

[29] Balog, R.; Jørgensen, B.; Nilsson, L.; Andersen, M.; Rienks, E.; Bianchi, M.; Fanetti, M.; Lægsgaard, E.; Baraldi, A.; Lizzit, S. et al. Bandgap opening in graphene induced by patterned hydrogen adsorption. *Nat. Mater.* **2010**, *9*, 315–319.

[30] Baringhaus, J.; Ruan, M.; Edler, F.; Tejeda, A.; Sicot, M.; Taleb-Ibrahimi, A.; Li, A. P.; Jiang, Z. G.; Conrad, E. H.; Berger, C. et al. Exceptional ballistic transport in epitaxial graphene nanoribbons. *Nature* **2014**, *506*, 349–354.

[31] Lee, S.-K.; Jang, H. Y.; Jang, S.; Choi, E.; Hong, B. H.; Lee, J. C.; Park, S. H.; Ahn, J.-H. All graphene-based thin film transistors on flexible plastic substrates. *Nano Lett.* **2012**, *12*, 3472–3476.

[32] Sun, D.-M.; Timmermans, M. Y.; Kaskela, A.; Nasibulin, A. G.; Kishimoto, S.; Mizutani, T.; Kauppinen, E. I.; Ohno, Y. Mouldable all-carbon integrated circuits. *Nat. Commun.* **2013**, *4*, 2302.

[33] Qi, J. S.; Huang, J. Y.; Feng, J.; Shi, D. N.; Li, J. The possibility of chemically inert, graphene-based all-carbon electronic devices with 0.8 eV gap. *ACS Nano* **2011**, *5*, 3475–3482.

[34] Chen, W.; Yu, Y. Y.; Zheng, X. M.; Qin, S. Q.; Wang, F.; Fang, J. Y.; Wang, G.; Wang, C. C.; Wang, L.; Peng, G. et al. All-carbon based graphene field effect transistor with graphitic electrodes fabricated by e-beam direct writing on PMMA. *Sci. Rep.* **2015**, *5*, 12198.

[35] Solomon, G. C.; Andrews, D. Q.; Van Duyne, R. P.; Ratner, M. A. When things are not as they seem: Quantum interference turns molecular electron transfer "rules" upside down. *J. Am. Chem. Soc.* **2008**, *130*, 7788–7789.

[36] Reuter, M. G.; Seideman, T.; Ratner, M. A. Molecular conduction through adlayers: Cooperative effects can help or hamper electron transport. *Nano Lett.* **2011**, *11*, 4693–4696.

[37] Soler, J. M.; Artacho, E.; Gale, J. D.; García, A.; Junquera, J.; Ordejón, P.; Sánchez-Portal, D. The SIESTA method for *ab initio* order-N materials simulation. *J. Phys.: Condens. Matter* **2002**, *14*, 2745–2779.

[38] Perdew, J. P.; Zunger, A. Self-interaction correction to density-functional approximations for many-electron systems. *Phys. Rev. B* **1981**, *23*, 5048–5079.

[39] Brandbyge, M.; Mozos, J.-L.; Ordejón, P.; Taylor, J.; Stokbro, K. Density-functional method for nonequilibrium electron transport. *Phys. Rev. B* **2002**, *65*, 165401.